

Energy flux analysis for quantification of vibratory pile driving efficiency

Gómez, Sergio S.; Tsetas, Athanasios; Metrikine, Andrei V.

DOI

[10.1016/j.jsv.2022.117299](https://doi.org/10.1016/j.jsv.2022.117299)

Publication date

2022

Document Version

Final published version

Published in

Journal of Sound and Vibration

Citation (APA)

Gómez, S. S., Tsetas, A., & Metrikine, A. V. (2022). Energy flux analysis for quantification of vibratory pile driving efficiency. *Journal of Sound and Vibration*, 541, Article 117299. <https://doi.org/10.1016/j.jsv.2022.117299>

Important note

To cite this publication, please use the final published version (if applicable). Please check the document version above.

Copyright

Other than for strictly personal use, it is not permitted to download, forward or distribute the text or part of it, without the consent of the author(s) and/or copyright holder(s), unless the work is under an open content license such as Creative Commons.

Takedown policy

Please contact us and provide details if you believe this document breaches copyrights. We will remove access to the work immediately and investigate your claim.

Contents lists available at [ScienceDirect](https://www.sciencedirect.com)

Journal of Sound and Vibration

journal homepage: www.elsevier.com/locate/jsvi

Energy flux analysis for quantification of vibratory pile driving efficiency

Sergio S. Gómez^{*}, Athanasios Tsetas, Andrei V. Metrikine

Faculty of Civil Engineering and Geosciences, Delft University of Technology, Stevinweg 1, 2628 CN Delft, The Netherlands

ARTICLE INFO

Keywords:

Pile installation
Energy flux
Shell dynamics
Wave propagation
Experimental campaign

ABSTRACT

In this paper, the energy flux in a pile modeled as an elastic shell, is studied theoretically and experimentally. Based on this analysis, a new procedure is proposed to quantify the pile installation efficiency. This procedure is of importance for vibratory installation of the foundations of offshore wind turbines and it is believed to be the first procedure that relies directly on the energy propagating down the pile rather than the energy supplied by the vibratory shaker. The proposed approach is tested on piles installed by two distinct vibratory techniques, i.e. the axial vibratory driving and the recently developed Gentle Driving of Pile (GDP) method. The field data obtained during an experimental campaign were analyzed with the proposed energy flux approach. The cumulative energy flux in the pile normalized by the energy input of the shaker is found to be the best measure for quantification of the installation efficiency. Correspondingly, the main proposition of this paper is that the installation efficiency will be maximized provided that the normalized cumulative energy flux is at its maximum.

1. Introduction

Offshore wind is one of the most propitious renewable energy resources [1]. The international sustainability targets require further growth of the offshore wind capacity, which leads to constant increase of the size of offshore wind turbines (OWTs), the distance to shore and the water depth of installation [2]. As a result, engineering challenges continuously arise in the construction of offshore wind farms and innovative solutions are needed to further improve the current design aspects and reduce the cost of offshore wind energy [3–5]. In the vast majority of the OWTs, bottom-fixed foundations are used to support them and amongst the available foundation concepts the monopile is the foremost one [6]. This foundation type is used in more than 80% of all the installed OWT foundations up to date in Europe [7] and comprises the optimal solution for water depths up to 40 m, while technical developments towards deeper waters are ongoing [8].

At present, impact piling is the most commonly used method for the installation of monopiles in the offshore environment [9]. However, this installation method is associated with major environmental concerns related to underwater noise emissions [10]. With increasing size of monopiles and reaching the capabilities of current design practices, it is essential that alternative methods with low environmental impact are developed for monopile installation. In view of these developments, the offshore industry is shifting its focus to vibratory techniques, such as the classical axial vibratory driving and the recently developed “Gentle Driving of Piles” (GDP) method [11,12]. However, the shift to the vibratory techniques introduces new challenges. As monopiles become larger and reach deeper waters, larger soil resistance is encountered during monopile installation. Therefore, the installation process has to be performed in an efficient manner to ensure that the available power supply of the vibratory device is adequate to successfully

^{*} Corresponding author.

E-mail addresses: s.sanchezgonzalez-1@tudelft.nl (S.S. Gómez), A.Tsetas@tudelft.nl (A. Tsetas), A.Metrikine@tudelft.nl (A.V. Metrikine).

<https://doi.org/10.1016/j.jsv.2022.117299>

Received 30 March 2022; Received in revised form 8 August 2022; Accepted 8 September 2022

Available online 15 September 2022

0022-460X/© 2022 The Author(s). Published by Elsevier Ltd. This is an open access article under the CC BY license (<http://creativecommons.org/licenses/by/4.0/>).

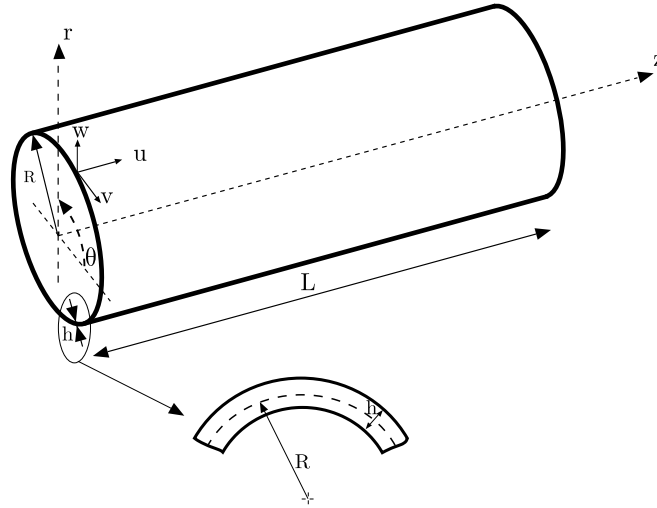


Fig. 1. Co-ordinate system and dimensions of a cylindrical shell.

drive the monopile into the seabed with low environmental impact. In order to select the appropriate installation technique, a framework to assess the pile driving efficiency is necessary. To the authors' knowledge, currently there is no established method to quantify the pile driving efficiency and its relation to the installation performance. To close this knowledge gap, this paper proposes a procedure based on the energy flux of the elastic waves in the pile to quantify vibratory pile driving efficiency. The energy flux analysis comprises an efficient and versatile approach employed in a vast range of studies regarding e.g. vibrations of thin plates with mean flow [13], vibration isolators [14] and damage identification in plate-like structures [15]. However, the energy flux has not been used in the past for quantification of the efficiency of the vibratory pile driving. In this paper, it is shown, for the first time, that the energy flux carried by elastic waves down the pile is directly related to the installation performance. To this end, the pile is first modeled as a thin cylindrical shell and an analytical expression for the energy flux is derived based on the Lagrangian density function. Then, the energy flux is computed based on data collected in an extensive experimental campaign during which axial vibratory driving and GDP were tested. The analysis showed that the cumulative energy flux provides clear information about the installation performance. Therefore, it is concluded that the energy flux method is an efficient tool to improve the process of pile installation.

This paper is organized as follows. In Section 2, the governing equations of thin cylindrical shell based on the membrane theory and the derivation of the energy flux in the pile are presented. Section 3 outlines the parts of the experimental campaign that are relevant to this paper. In Section 4, the power and energy input delivered by the Hydraulic Power Units (HPUs) of the shakers used in the experiments are given for the examined cases. The results of the energy flux analysis are presented in Section 5, accompanied by relevant experimental data obtained during the installation tests. Finally, Section 6 concludes this paper with a discussion of the results and their added value for the theoretical understanding of vibratory pile installation.

2. A cylindrical membrane shell model

In order to derive an energy flux expression for a thin cylindrical shell, the kinematic and constitutive relations are first established. To this end, a uniform thin cylindrical shell is considered, with finite length L , radius R , and wall thickness h , as shown in Fig. 1. A cylindrical reference system (r, θ, z) is employed throughout this work (see Fig. 1).

2.1. Kinematic and constitutive equations

The displacement vector $\mathbf{u} = [u_r, u_\theta, u_z]$ of a material point in a cylindrical shell with components u_r, u_θ, u_z is given, according to the membrane shell theory [16], as follows,

$$\begin{aligned} u_r(r, \theta, z, t) &= w(\theta, z, t) \\ u_\theta(r, \theta, z, t) &= v(\theta, z, t) \\ u_z(r, \theta, z, t) &= u(\theta, z, t) \end{aligned} \quad (1)$$

where $u = u(\theta, z, t)$, $v = v(\theta, z, t)$ and $w = w(\theta, z, t)$ are the displacements of an arbitrary point in the middle surface of the shell in the axial, circumferential and radial directions, respectively. Given the displacement field presented in Eq. (1), the position

of any material point in the shell is governed by the three components of the displacement vector of the middle surface. The strain–displacement relations are given as follows:

$$\begin{aligned}\varepsilon_{zz} &= \frac{\partial u_z}{\partial z} = \frac{\partial u}{\partial z} \\ \varepsilon_{\theta\theta} &= \frac{u_r}{R} + \frac{1}{R} \frac{\partial u_\theta}{\partial \theta} = \frac{w}{R} + \frac{\partial v}{R\partial\theta} \\ \gamma_{z\theta} &= \frac{1}{R} \frac{\partial u_z}{\partial \theta} + \frac{\partial u_\theta}{\partial z} = \frac{\partial v}{\partial z} + \frac{1}{R} \frac{\partial u}{\partial \theta}\end{aligned}\quad (2)$$

In accordance with Love's first approximation shell theories, the rest of the strain components are $\varepsilon_{rr} = \gamma_{rz} = \gamma_{r\theta} = 0$ [17]. Based on the generalized Hooke's law, the stress–strain relations can be written as,

$$\begin{aligned}\sigma_{zz} &= \frac{E}{1-\nu^2} (\varepsilon_{zz} + \nu\varepsilon_{\theta\theta}) \\ \sigma_{\theta\theta} &= \frac{E}{1-\nu^2} (\varepsilon_{\theta\theta} + \nu\varepsilon_{zz}) \\ \tau_{z\theta} &= \frac{E}{2(1+\nu)} \gamma_{z\theta}\end{aligned}\quad (3)$$

where E and ν are the Young's modulus and Poisson ratio of the shell material, respectively. Conclusively, the remaining stress components are $\sigma_{rr} = \tau_{rz} = \tau_{r\theta} = 0$, in accordance with the third and fourth postulates of Love's first approximation.

2.2. Energy balance equation

The balance of the mechanical energy for a segment Ω of a cylindrical membrane shell reads [18]:

$$\frac{d\mathcal{E}(t)}{dt} + P(t) + W_{\text{diss}}(t) = W_{\text{ext}}(t) \quad (4)$$

where $\mathcal{E}(t)$ is the mechanical energy of the segment Ω , $P(t)$ is the energy that crosses the boundary Γ of the segment Ω per unit time, $W_{\text{ext}}(t)$ is the energy that is introduced into the segment Ω by external forces per unit time and $W_{\text{diss}}(t)$ is the energy dissipated in the segment Ω per unit time. These scalar quantities in Eq. (4) can be expressed as:

$$\begin{aligned}\mathcal{E}(t) &= \int_{\Omega} e(\theta, z, t) d\Omega \\ P(t) &= \int_{\Gamma} \mathbf{s}(\theta, z, t) \mathbf{n} d\Gamma \\ W_{\text{diss}}(t) &= \int_{\Omega} w_{\text{diss}}(\theta, z, t) d\Omega \\ W_{\text{ext}}(t) &= \int_{\Omega} \mathbf{f}_{\text{ext}}(\theta, z, t) \dot{\mathbf{u}} d\Omega\end{aligned}\quad (5)$$

where e is surface density of the mechanical energy, \mathbf{s} is the energy flux through the boundary per unit length, \mathbf{f}_{ext} is the surface density of the external forces and w_{diss} is the surface density of the dissipated energy. The energy density e is defined as:

$$e = e_k + e_p = \frac{1}{2} \rho (\dot{u}_z^2 + \dot{u}_\theta^2 + \dot{u}_r^2) + \frac{1}{2} (\sigma_{zz}\varepsilon_{zz} + \sigma_{\theta\theta}\varepsilon_{\theta\theta} + \tau_{z\theta}\gamma_{z\theta}) \quad (6)$$

where e_k and e_p are the kinetic and strain energy densities, respectively, and ρ is the mass density of the shell material. The Lagrangian surface density function λ is obtained by using Eqs. (1)–(3) and integrating over the thickness h of the shell as follows:

$$\begin{aligned}\lambda &= \int_{R-\frac{h}{2}}^{R+\frac{h}{2}} (e_k(r, \theta, z, t) - e_p(r, \theta, z, t)) dr = \\ &\quad \frac{\rho h}{2} (\dot{u}^2 + \dot{v}^2 + \dot{w}^2) - \frac{Eh}{2(1-\nu^2)} \left(\varepsilon_{\theta\theta}^2 + \varepsilon_{zz}^2 + 2\nu\varepsilon_{\theta\theta}\varepsilon_{zz} + \frac{1-\nu}{2}\gamma_{z\theta}^2 \right)\end{aligned}\quad (7)$$

The expression for the energy flux in Eq. (5) is obtained using the Lagrangian formalism; the latter treatment is summarized in Appendix. By applying Eq. (A.11) the z component of the energy flux s_z can be written as:

$$s_z(\theta, z, t) = \frac{\partial \lambda}{\partial u_z} \dot{u} + \frac{\partial \lambda}{\partial v_z} \dot{v} + \frac{\partial \lambda}{\partial w_z} \dot{w} = -D_0 \left\{ (\varepsilon_{zz} + \nu\varepsilon_{\theta\theta}) \dot{u} + \frac{1-\nu}{2} \gamma_{z\theta} \dot{v} \right\} \quad (8)$$

In this work, the main objective is to analyze the energy flowing along the z -axis and to evaluate the energy used to penetrate the pile into the soil. The load applied to the membrane shell is considered axisymmetric in our investigation. Therefore, we assume the shell response to be axisymmetric too, i.e. $\frac{\partial(\cdot)}{\partial\theta} = 0$. Under this assumption, the energy $P(t)$ that flows through a cross-section ($z = \text{constant}$) of the shell per unit time can be expressed as:

$$P(t) = \int_0^{2\pi R} s_z(\theta, z = \text{constant}, t) d\theta = -2\pi R D_0 \left\{ (\varepsilon_{zz} + \nu\varepsilon_{\theta\theta}) \dot{u} + \frac{1-\nu}{2} \gamma_{z\theta} \dot{v} \right\} \quad (9)$$

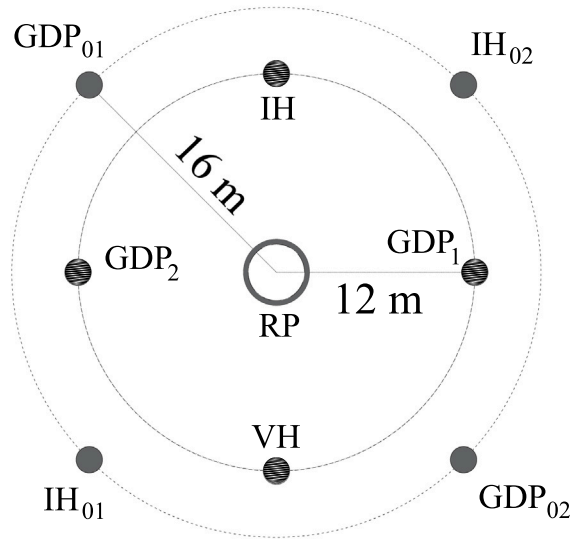


Fig. 2. Pile installation layout.

Table 1
Pile properties.

Length [m]	Outer diameter [m]	Thickness [m]	Total pile mass [kg]
10	0.762	0.0159	2907

where

$$D_0 = \frac{Eh}{1 - \nu^2} \quad (10)$$

Finally, it is assumed that the external forces are provided only by the shaker.

3. GDP experimental campaign

The focus of this work lies in the analysis of the GDP field tests, by means of the energy flux method that was outlined in Section 2. Further aspects of pile installation apart from penetration rate and energy efficiency (e.g. post-installation stiffness) are also of importance; the latter aspects of the present pile tests are discussed in other works [11,12]. During the installation phase of the experimental campaign, several piles with $R = 0.37$ m (approximately 1:10 compared to offshore monopiles) were installed. The test site was found to be comprised by medium to medium-dense sand and was located in Maasvlakte II at the Port of Rotterdam (The Netherlands). In total, eight test piles (TP) were installed during the installation phase, around one reaction pile (RP) in the configuration shown in Fig. 2.

Out of the eight test piles four of them were instrumented, while the remaining four uninstrumented piles were used for auxiliary testing purposes. From the four instrumented piles, two of the piles were installed by means of the GDP technique, one pile was installed by means of the conventional axial vibratory hammer (VH) and one pile was installed via the impact hammer technique (IH). To carry out the investigation presented in this work, we focus on the instrumented piles driven by the vibratory techniques, thus the study of the impact hammer pile (IH) is out of the scope of this paper. The dimensions of the installed test piles are given in Table 1.

The final penetration of the piles was 8 m and an identical protocol was followed for consistency and comparison purposes. First, each pile was supported and guided by a rig and a crane to drive the pile up to approximately 3 m into the soil. Subsequently, the pile rig was removed and the tension applied by the crane was released. As a final step, the pile was driven into the soil via the shaker excitation. In order to have a fair comparison between the vibratory techniques, all the results presented in this paper focus on the final stage of the installation (i.e. the last 5 m of the penetration).

With a view to offshore monopile installation, it should be noted that lower L_{embed}/D ratios (compared to the present tests) are encountered offshore. This is expected as large-diameter piles are used offshore and sufficient (for pile bearing capacity) embedment depth is reached for smaller L_{embed}/D ratios. However, for small- and medium-scale tests larger L_{embed}/D ratios are necessary to reach a sufficient embedment depth and obtain meaningful results from the installation process. In general, plugging effects are not likely to occur during offshore pile driving [19] and even less during vibro-driving (compared to impact hammering). For the size of the piles in the GDP campaign, plugging was not expected, based on installation tests of similar scale by Henke and Grabe

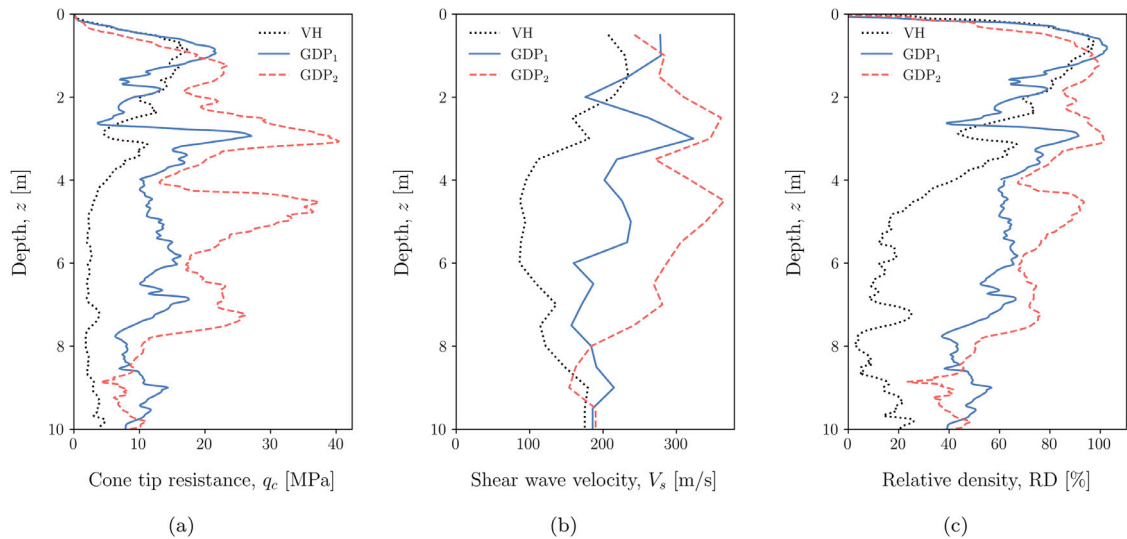


Fig. 3. Profiles of (a) cone tip resistance (q_c), (b) shear wave velocity (V_s), and (c) relative density (RD) obtained at the TP locations from the *in-situ* SCPTu tests.

[20]. An additional note, focused on offshore monopiles, is that the increase in pile diameter leads to increased radial pile motion during driving (ring frequency effect) [21], which can reduce the installation efficiency as well as affect the post-installation soil state. Evidently, further experimental tests with piles of larger diameter are required to investigate such effects in more detail.

3.1. Geotechnical site investigation

In order to characterize the soil profiles at the locations of installation, an extensive geotechnical investigation was conducted at the test site. To this end, cone penetration tests with pore water pressure measurements (CPTu) were performed initially in multiple locations of the test site. This set of tests served to determine the final installation locations of the four instrumented piles. At the final four selected locations, Seismic CPTu (SCPTu) tests were performed in order to obtain further information about the dynamic properties of the soil profiles.

In Fig. 3 the cone tip resistance (q_c), shear wave velocity (V_s), and relative density (RD) are presented for the locations at which the VH and GDP piles were installed. The SCPTu tests were performed up to a target depth of 10 m. The results presented in Fig. 3 were obtained using the approach outlined by Jamiolkowski et al. [22]. The depth of ground water table during the site investigation ranged from 3.5 m to 4.5 m. Therefore, the field data analyzed in this paper, correspond for the most part of the installation to water-saturated soil layers. According to the relative density profiles shown in Fig. 3(c), the site comprised very dense sand (RD = 80–100%) in the upper 5 m, and medium-dense to dense sand (RD = 60–80%) in the lower 5 m. A deviation from these observations can be seen at the location of the VH pile, where the SCPTu data indicate much lower cone tip resistance and relative density (RD < 40%) in the lower 5 m. That result is considered to be favorable for the VH pile in terms of installation performance, as the resistance encountered in that soil layer was expected to be significantly lower compared to the GDP locations.

3.2. Description of the GDP shaker

The use of vibratory devices for installation of piles in onshore conditions is well-known and established for sheet and pipe piles [23]. However, the design of a vibratory device capable of generating simultaneous vertical and torsional excitation comprised a challenge on its own. For that purpose, during the GDP project, one of the first and foremost tasks was the design of the GDP shaker. This novel pile driving technology is envisaged to increase the efficiency of offshore monopile installation and reduce the environmental impact (noise emissions) compared to conventional impact piling. The main novelty of this technique lies in the introduction of high-frequency torsional motion as the main pile driving mechanism; high-frequency here is understood as appreciably higher than the regular frequency levels encountered in standard axial vibratory driving. In conjunction with the conventional (low-frequency) axial excitation, this method constitutes what we define as the GDP technique. The introduction of the high-frequency torsional motion aims to achieve low levels of noise emission, reduce fatigue levels in the pile and increase the penetration speed.

Both the GDP shaker and the axial vibratory device, hereafter referred to as CV-25, operate on the same principle of eccentric rotating masses. The resultant dynamic excitation forces the pile into the soil. In the case of the GDP shaker apart from the standard set of eccentric masses for the vertical excitation, an additional configuration is needed to generate the dynamic torsional moment. The latter is achieved by using two exciter blocks in diametrically opposite locations, that generate a force couple resultant. This



Fig. 4. The GDP shaker (left) and the Axial vibro-hammer CV-25 (right).

Table 2
Technical specifications of the GDP shaker.

	GDP shaker		Axial vibro-hammer CV-25
	Axial shaker	Torsional shaker	Axial shaker
Mass [kg]		5150	4100
Eccentric moment [kgm]	15	4	25
Rotational speed [rpm]	1400	4800	1800
Operational power [kW]	72	188	204
Maximum power [kW]	150	390	263

force couple is uniformly distributed along the pile circumference, so as to create a torque, as these two blocks are mounted on a support structure that is connected to the pile via a bolted flange connection. The same connection was also used for the case of axial vibratory driving. In Fig. 4, both the GDP shaker and CV-25 are shown, while the main technical specifications of the shakers are summarized in Table 2.

The design of the GDP shaker was based on the principles of the GDP method, albeit subject to constraints by practical limitations. Specifically, the axial vibration frequency of GDP was set similar to the one used in axial vibro-driving, in order to showcase the effect of torsional vibrations. For the GDP torsional frequency, the upper limit was defined such that the total power capacity of the GDP shaker was comparable to CV-25. Therefore, the final design of the GDP shaker led to axial and torsional loading with (nominal) frequencies up to 23 Hz and 80 Hz, respectively.

3.3. Instrumentation set-up

The two GDP piles and the VH pile were instrumented in the same manner. The instrumentation of all piles consisted of 2 tri-axial accelerometers of MEMS type, 24 uni-directional (in-line) strain sensors, 6 rosette shape strain sensors and 2 temperature sensors of the fiber optics grating (FBG) type, per pile. The sensor specifications are summarized in Table 3. In all three piles, the MEMS accelerometers as well as the FBGs were installed to the outside wall of the pile at diametrically opposed locations. The disposition of the sensors along the longitudinal direction in the piles is shown in Fig. 5.

The pile instrumentation strategy is aligned to one of the main goals of this work, which is quantification of the energy delivered by the hydraulic power unit (HPU) that is flowing into the pile during the driving process. To this end, the data collected by the sensors installed at the top of the pile ($L_1 = 1.56$ m) are used. The position of the sensors at L_1 is selected customarily to avoid any potential failure by placing the sensors too close to the pile flange.

3.4. Experimental data interpretation

The energy flux can be computed using the strains recorded by the rosette FBG's and the velocities obtained from the acceleration measurements, respectively. Due to the general character of application of the sensors, in most cases, post-processing of these data is necessary. Let us begin with the strain measurements recorded by the FBG rosettes, shown in Fig. 5. The FBG sensors were installed at the locations P and Q defined by the following coordinates respectively, $\{r = R + h/2, \theta = 0^\circ, z = L_1\}$ and $\{r = R + h/2, \theta = 180^\circ, z = L_1\}$. At each location of the FBG sensors we define three strain components as shown in Fig. 6, i.e. $\varepsilon_{\psi_1}^{P:Q}$, $\varepsilon_{\psi_2}^{P:Q}$ and $\varepsilon_{\psi_3}^{P:Q}$, where $\psi_1 = 0^\circ$, $\psi_2 = 60^\circ$ and $\psi_3 = 120^\circ$ with respect to the z -coordinate. These strains are related to the strains in the original reference system as:

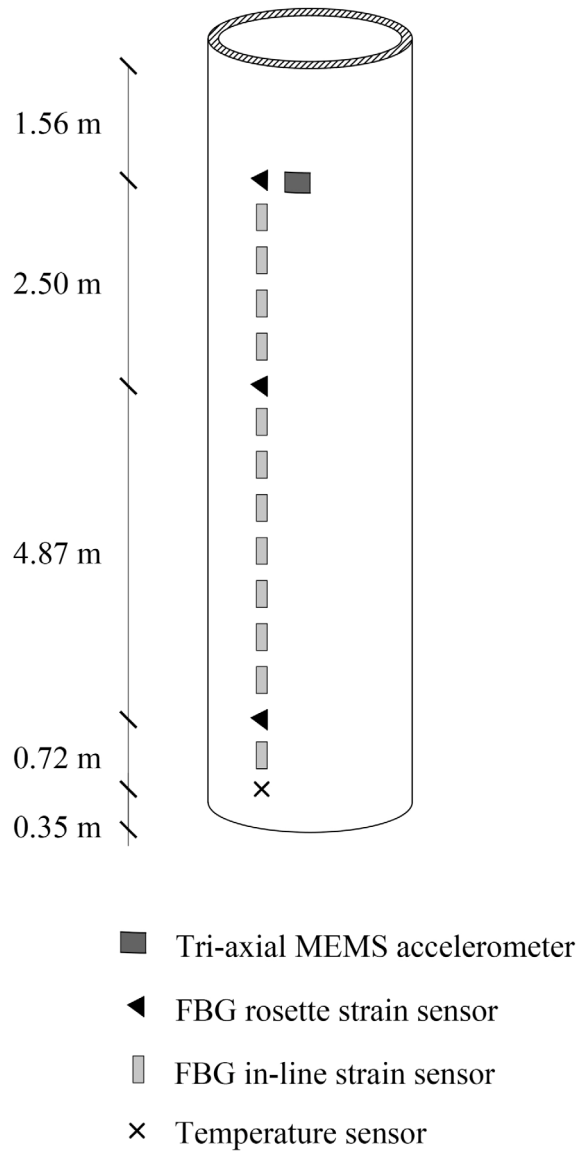


Fig. 5. Instrumentation of piles GDP 1, GDP 2 and VH.

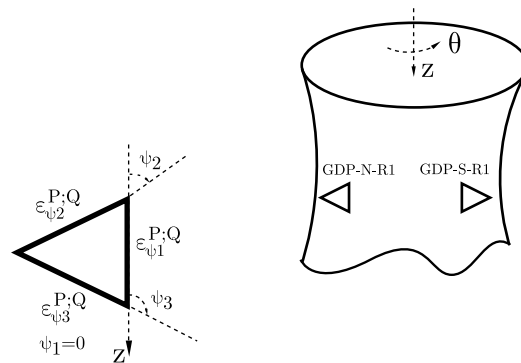


Fig. 6. Positioning of the rosette shape strain gauges with respect to the shell reference axis.

Table 3
Technical specifications of in-line FBG strains sensors and temperature sensors.

Type of accelerometer	MEMS ADXL377
Number of sensors per pile	2 (1 per side)
Measurement range	±200 g
Bandwidth (x, y axes)	0.5 Hz–1300 Hz
Bandwidth (z axis)	0.5 Hz–1000 Hz
Sensitivity (x axis)	5.8 mV/g
Sensitivity (y axis)	6.5 mV/g
Sensitivity (z axis)	7.2 mV/g
Type of FBG strain sensor	Sylex FFA-01
Number of sensors per pile	24 (12 per side)
Measurement range	±3000 μm/m
FBG wavelength range	1510 nm–1590 nm
Fiber coating	Polyimide
Type of temperature sensor	Sylex TPA-01
Number of sensors per pile	2 (1 per side)
Measurement range	−20 °C–80 °C
Measurement accuracy	1 °C
Measurement precision	0.2 °C

$$\varepsilon_{\psi_i}^{P:Q} = \mathbf{u}_i^T \mathbf{D} \mathbf{u}_i, \quad i = 1, 2, 3 \quad (11)$$

where,

$$\mathbf{u}_i = \begin{bmatrix} \cos(\psi_i) \\ \sin(\psi_i) \end{bmatrix}, \quad \mathbf{D} = \begin{bmatrix} \varepsilon_{zz} & \frac{1}{2}\gamma_{z\theta} \\ \frac{1}{2}\gamma_{z\theta} & \varepsilon_{\theta\theta} \end{bmatrix} \quad (12)$$

Expanding Eq. (11), the three measured strain components are expressed as:

$$\begin{aligned} \varepsilon_{\psi_1}^{P:Q} &= \varepsilon_{zz} \cos^2(\psi_1) + \varepsilon_{\theta\theta} \sin^2(\psi_1) + \gamma_{z\theta} \cos(\psi_1) \sin(\psi_1) \\ \varepsilon_{\psi_2}^{P:Q} &= \varepsilon_{zz} \cos^2(\psi_2) + \varepsilon_{\theta\theta} \sin^2(\psi_2) + \gamma_{z\theta} \cos(\psi_2) \sin(\psi_2) \\ \varepsilon_{\psi_3}^{P:Q} &= \varepsilon_{zz} \cos^2(\psi_3) + \varepsilon_{\theta\theta} \sin^2(\psi_3) + \gamma_{z\theta} \cos(\psi_3) \sin(\psi_3) \end{aligned} \quad (13)$$

By means of the measured strains $\varepsilon_{\psi_1}^{P:Q}$, $\varepsilon_{\psi_2}^{P:Q}$ and $\varepsilon_{\psi_3}^{P:Q}$, the components of the matrix \mathbf{D} , which comprise the strains in the original reference system, can be derived from Eq. (13).

The remaining measurements that are necessary to compute the energy flux are the velocities, which are retrieved from the accelerations via numerical integration. In all three piles, there were two accelerometers $a^{P:Q}$ located at the aforementioned positions P and Q next to the rosette FBGs, as shown in Fig. 5. These sensors recorded acceleration data in three orthogonal directions $\mathbf{a}^{P:Q} = [a_{x'}, a_{y'}, a_{z'}]$, in a reference system (x', y', z') . Finally, these accelerometers were positioned such that $a_z^{P:Q} = a_{z'}^{P:Q}$, $a_r^{P:Q} = a_{x'}^{P:Q}$ and $a_\theta^{P:Q} = \frac{1}{R} a_{y'}^{P:Q}$.

4. Power input to the piles

In this section, the power input $W_{\text{ext}}(t)$ to the piles by two different vibratory techniques is provided directly from the logging system of the HPUs used in the field tests. According to the GDP shaker specifications, two independent exciter blocks are used for the vertical and the torsional excitations. Each exciter block is powered by its own HPU, such that torsional and axial vibrations are generated independently. In Fig. 7, the power inputs delivered by the exciter blocks that induce the vertical vibrations in the VH and GDP shakers are plotted versus time. Similarly, the power delivered by the HPUs of the torsional counterpart of the GDP shaker are computed and presented in Fig. 8. Furthermore, Figs. 9 and 10 provide the power consumption in terms of the penetration depth.

It is readily apparent that the power delivered to impose torsional vibration is appreciably higher than its axial counterpart for both GDP₁ and GDP₂. As regards to the axial vibratory excitation, the relevant HPU power consumed is almost identical for both GDP piles. However, the power consumed for torsional loading is appreciably higher for GDP₂, as a likely outcome of the denser soil profile at the location, which is also testified by the longer installation time. The latter statement is based on the fact that soil conditions (e.g. large soil reaction) can affect the power consumption, which occurs in vibratory driving due to the vibrator–pile–soil interaction [23] and can even lead to pile refusal [24]. Further, a drop in torsional power consumption is visible for GDP₂ between 50 s to 100 s (4 meters penetration in Fig. 10), which can be the result of a (temporary) reduction in soil resistance, as the power was delivered to maintain a given vibration frequency. The power consumed by the axial component slightly decreased with time and penetration depth, while the torsional counterpart increased for both piles. These trends indicate altogether that torsion is the main mechanism that overcomes the soil resistance to pile driving. The latter remark strongly affirms one of the basic assumptions of GDP driving, i.e. the significant effect of torsion on overcoming the frictional shaft resistance.

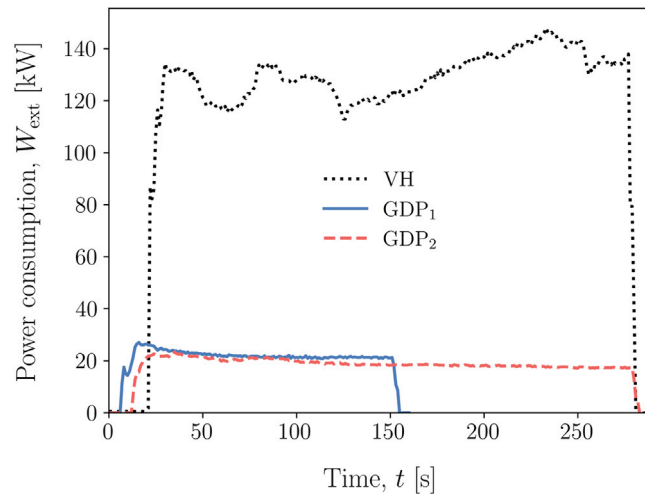


Fig. 7. Power consumption of the HPU for the vertical excitation (both VH and GDP).

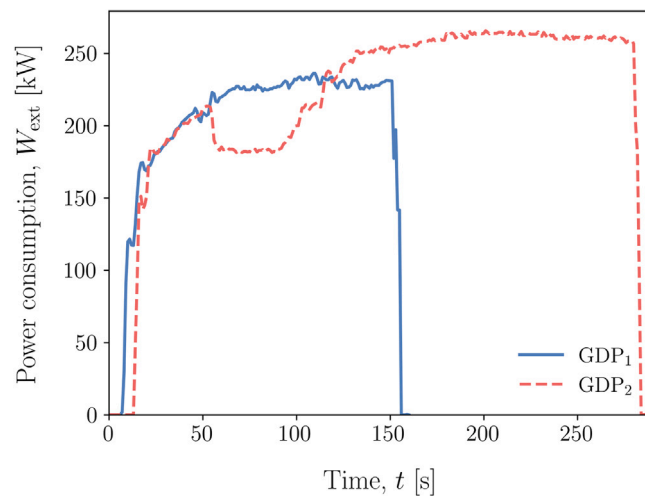


Fig. 8. Power consumption of the HPU for the torsional excitation (only GDP).

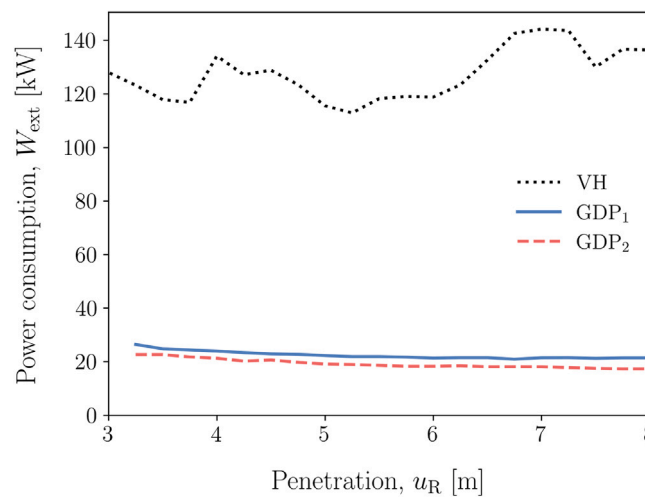


Fig. 9. Power consumption of the HPU with penetration depth for the vertical excitation (both VH and GDP).

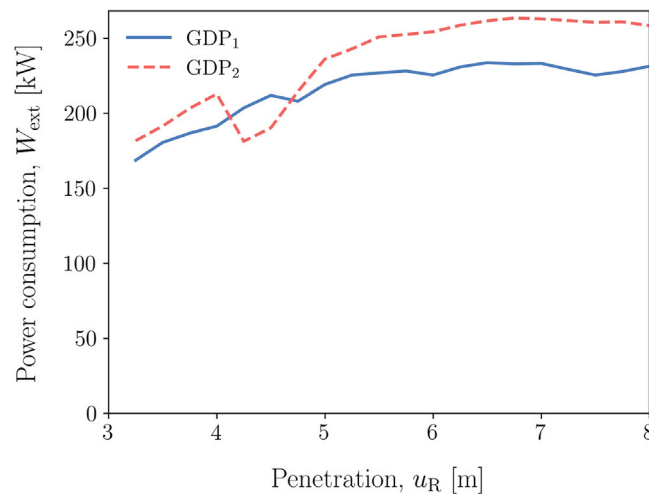


Fig. 10. Power consumption of the HPU with penetration depth for the torsional excitation (only GDP).

In the case of the axial vibratory shaker, one HPU is used to power the exciter block that generates the vertical excitation. In Fig. 7, it can be observed that the consumed power is quite constant for the first 100 s, approximately. From that moment, the power delivered by the HPU has a continuous slight increase until approximately the last 30 s, that the power slightly decreases. The site investigation data (Fig. 3) indicate that soil resistance at the location of the VH pile reduces drastically below 3 m, albeit the pile transitions from an unsaturated to a water-saturated layer, which may explain the power trend of the axial vibratory shaker. In general, it should be noted that the soil resistance at the location of the VH pile is significantly lower compared to the ones of the GDP piles.

5. Results

5.1. Experimental campaign results

Prior to the results of the energy flux analyses, the main experimental results that are relevant to this paper are presented. The plots presented hereafter correspond to the experimental data collected by the sensors located at the top side of the pile ($L_1 = 1.56$ m). The quantities that dominate the energy content for the VH pile are clearly the axial stresses and velocities, while for GDP both axial and in-plane shear stresses and velocities need to be considered. At this point, it is noted that all the analyses refer to the pile installation tests from the initial embedment of 3 m to the final embedment of 8 m.

The discrete Fourier transforms (DFTs) of the axial and circumferential accelerations are shown in Figs. 11 and 12. In Figs. 13 and 14, the axial (ϵ_{zz}) and in-plane shear (only GDP) ($\gamma_{z\theta}$) strains at the pile top are presented in the form of time series, in order to have a better view of the axial and torsional input excitations for the different piles. It is evident that both GDP piles have similar axial input (slightly larger in GDP₂), while in the case of GDP₂ the torsional input is clearly higher. Furthermore, the axial excitation for the VH pile is appreciably larger compared to GDP piles, as was expected due to higher eccentric moment and axial driving frequency. Similarly, the DFTs of the axial (ϵ_{zz}) and shear ($\gamma_{z\theta}$) strains recorded in all instrumented piles are presented in Figs. 15 and 16. As can be seen in both strain and acceleration spectra, the highest amplitude of axial and circumferential motion is found at the frequency of the vertical and torsional excitation, respectively.

A notable finding during the installation tests, that may provide additional insight in the mechanisms at play during vibratory driving, was the identification of super-harmonics with high amplitude in the pile response. Specifically, the axial quantities (strains and accelerations) of both VH and GDP piles showcase strong presence of super-harmonic components of the fundamental excitation frequencies in their spectra. For GDP a remark that requires even closer attention in view of the future development of the GDP method, is the identification in the axial spectra of frequencies related not only to the axial but also to the torsional loading. The implications of these results can aid to explain various open questions in the complex pile–soil response during vibratory installation.

The drivability performance of the driven piles is assessed based on the measured penetration rate. In Fig. 17, the penetration of the VH and the GDP piles is shown, measured via a potentiometer and an installation logging system. The former recording is considered more reliable as the sampling frequency of that sensor was equal to 1 kHz. However, the “slow” recording of the logging system (per 25 cm of penetration) can also be considered adequate based on the average penetration rates obtained for each pile (see Fig. 17). It is noted that during the installation of pile GDP₂ the potentiometer failed, thus such measurements for GDP₂ are not available.

As can be observed in Fig. 17, GDP₁ had a higher penetration rate compared to VH and GDP₂. Considering that both GDP piles were installed with identical settings, i.e. amplitude and frequency, the higher penetration rate of GDP₁ is evidently a result of the

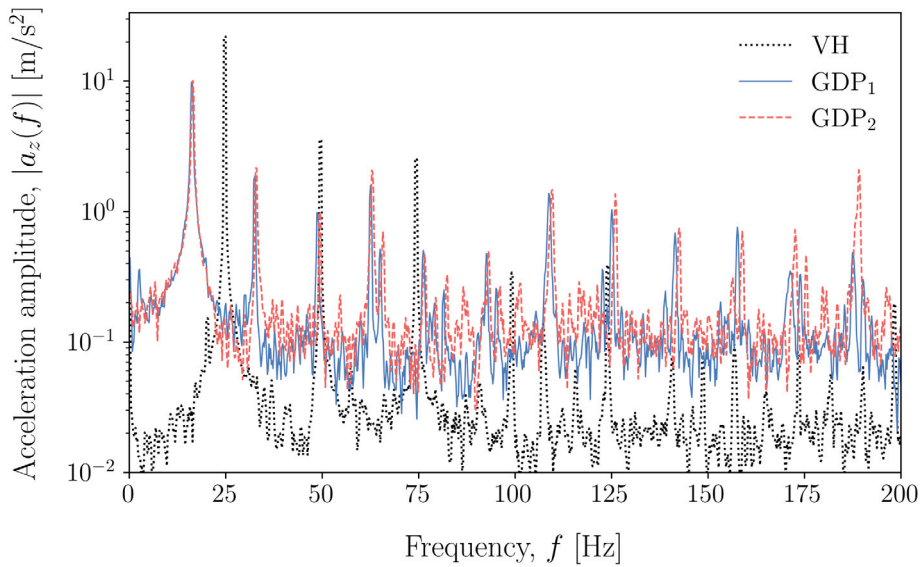


Fig. 11. Amplitude spectrum of the acceleration for piles VH, GDP₁ and GDP₂ in the axial direction.

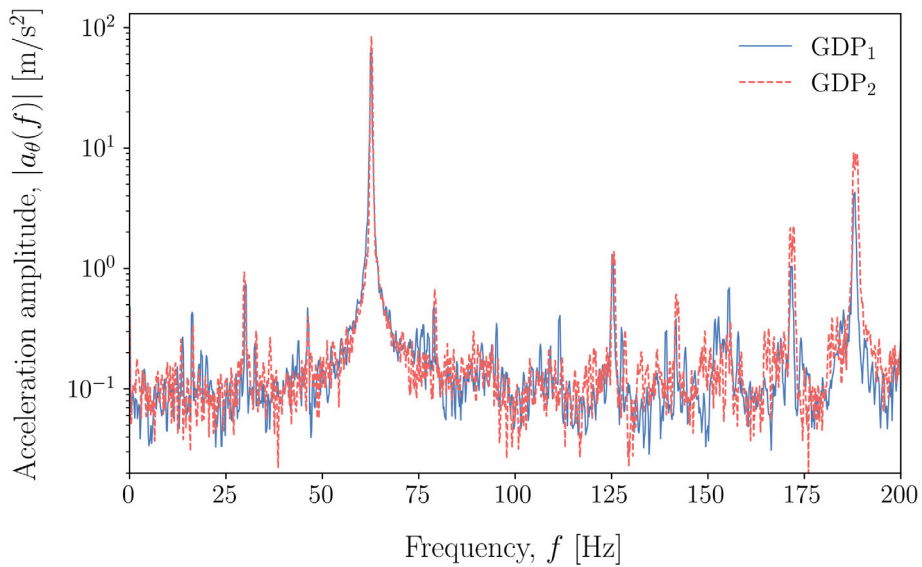


Fig. 12. Amplitude spectrum of the acceleration for piles GDP₁ and GDP₂ in the circumferential direction.

different soil conditions between the two pile locations. As can be observed in Fig. 3 the soil profile in the location of GDP₂ is significantly stiffer compared to that of GDP₁. In view of the importance of the soil resistance, it is interesting to note that although VH was installed in a notably weaker soil compared to GDP₁, it reached a significantly lower average penetration rate. Furthermore, GDP₂ was driven into the stiffest soil profile and yet its average penetration rate was approximately the same as that of VH (see Fig. 17). These observations support the statement that the introduction of the torsional excitation indeed increase the penetration speed of GDP₁.

5.2. Results of energy flux analysis

In this section, results of the energy flux calculations for the three instrumented piles, namely GDP₁, GDP₂ and VH are presented and discussed. Subsequently, the efficiency of two distinct vibratory pile driving techniques is quantified by means of the energy flux analysis. Figs. 18–20 show the energy flux along the longitudinal axis z computed at $z = L_1$, as a function of time for piles GDP₁, GDP₂ and VH, respectively. As can be seen in these plots the energy flux in all piles is quite different. Notably, the flux in

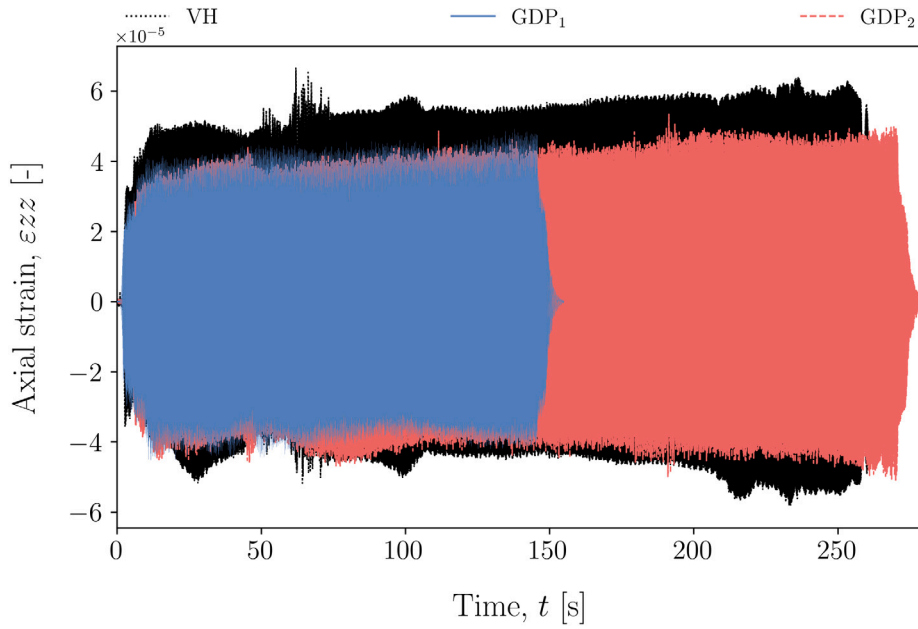


Fig. 13. Axial strain ε_{zz} at the pile top during installation for VH, GDP₁ and GDP₂.

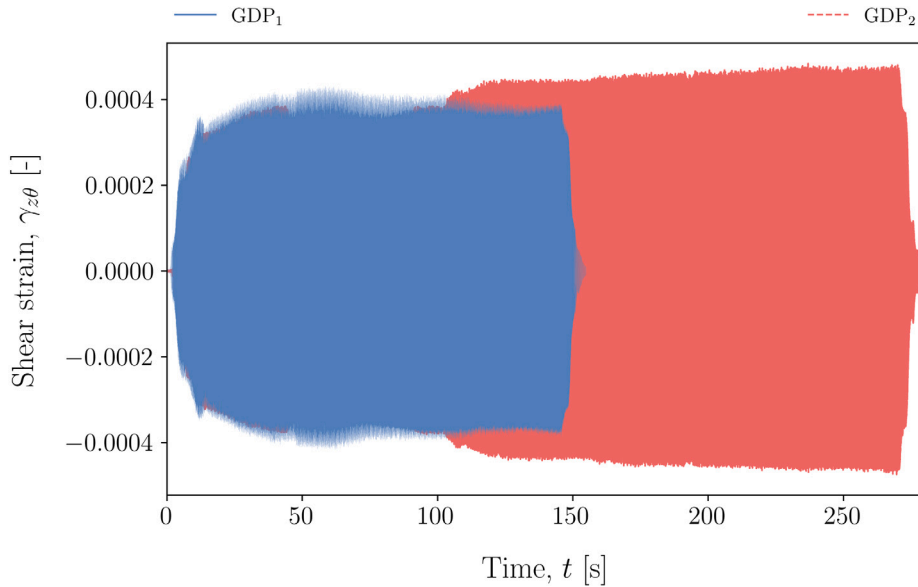


Fig. 14. In-plane shear strain $\gamma_{z\theta}$ at the pile top during installation for GDP₁ and GDP₂.

the VH pile is substantially lower in amplitude compared to that in the GDP piles. Fig. 18 demonstrates a distinct increase in the mean energy flux with pile penetration for pile GDP₁, while for GDP₂ the energy flux first increases and then decreases. In contrast to the visible trends of the GDP piles, the flux in the VH does not show any clear trend.

In order to understand further these observations, one needs to consider the corresponding penetration rates (Fig. 17), the cumulative energy flux into the pile (Fig. 21) and power input to the shakers. The latter is accounted for as a normalization factor to the cumulative energy flux. The ratio of the cumulative energy flux to the input energy is referred to as the driving efficiency and is plotted in Fig. 22 for piles VH, GDP₁ and GDP₂. Figs. 21 and 22 show a distinct and superior feature of the GDP₁ driving, namely a monotonic increase of the cumulative energy flux (dashed line in Fig. 21) which is accompanied by a nearly constant energy efficiency (dashed line in Fig. 22). This increase of $\int P(t)dt$ means that the energy introduced into the pile by the shaker is efficiently transmitted into the soil. In principle, the waves that travel down the pile rather transmit to the soil than reflect. This

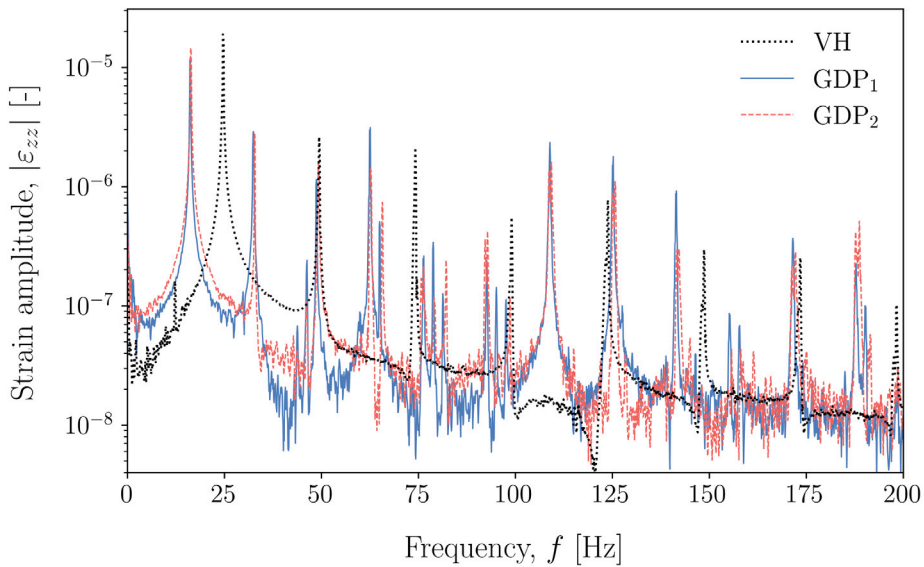


Fig. 15. Amplitude spectrum of axial strain ε_{zz} at the pile top for VH, GDP₁ and GDP₂.

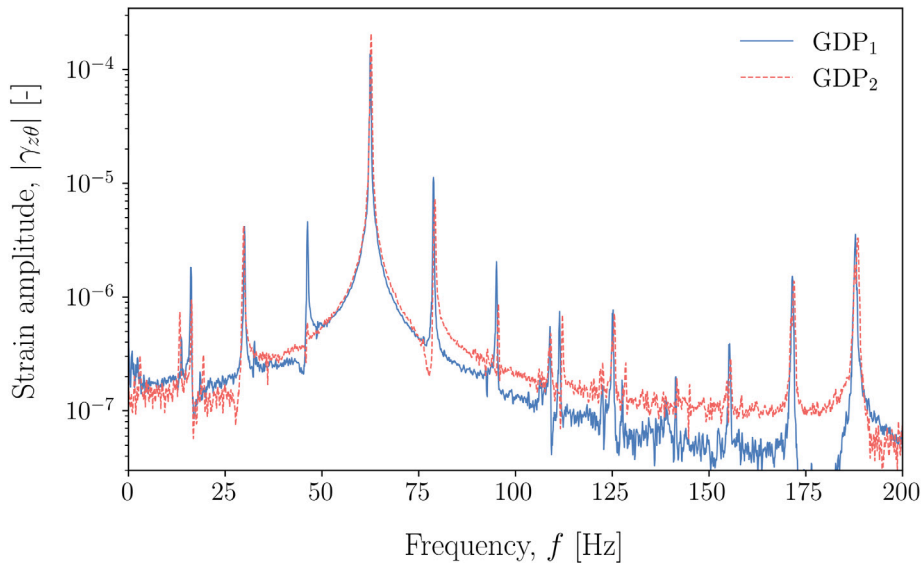


Fig. 16. Amplitude spectrum of in-plane shear strain $\gamma_{z\theta}$ at the pile top for GDP₁ and GDP₂.

situation corresponds, in our view, to a minor impedance contrast at the pile–soil interface (predominantly close to the pile tip). This reduced impedance contrast is not a property of the pile and soil alone, but comprises mainly a result of the pile vibrations that induce change of the soil impedance. As Fig. 17 shows this situation, i.e. the increase in the cumulative energy flux and the associated reduced impedance contrast, corresponds to the superior penetration rate.

As regards the penetration of the piles GDP₂ and VH a non-monotonic cumulative energy flux is observed. As can be seen in Fig. 21, the cumulative energy flux decreases after 6.0 m penetration depth for both VH and GDP₂. This decrease means that on average, the energy flows upwards in the pile, indicating a high and undesirable impedance contrast between the pile and the soil. This observed behavior is accompanied by a reduced penetration rate compared to GDP₁. The discrepancy between VH and GDP piles is accredited to the installation method, as the GDP soil profiles were significantly stiffer than VH and still GDP piles showcased higher efficiency ratios. The different behavior observed between GDP piles can only be accredited to the stiffer soil profile in the location of GDP₂, as the pile properties and the installation settings were virtually the same. However, the remarkable drop in driving efficiency in GDP₂ below the penetration depth of 4 m (Fig. 22) and the dissimilar pattern from GDP₁ can be considered an indication of reaching the GDP shaker capabilities for these installation settings. The obtained results and the provided interpretations allow

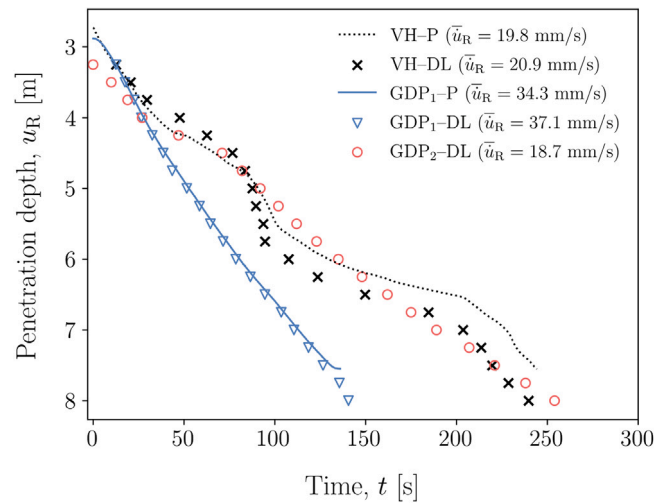


Fig. 17. Pile penetration for VH, GDP₁ and GDP₂ and average penetration rates.

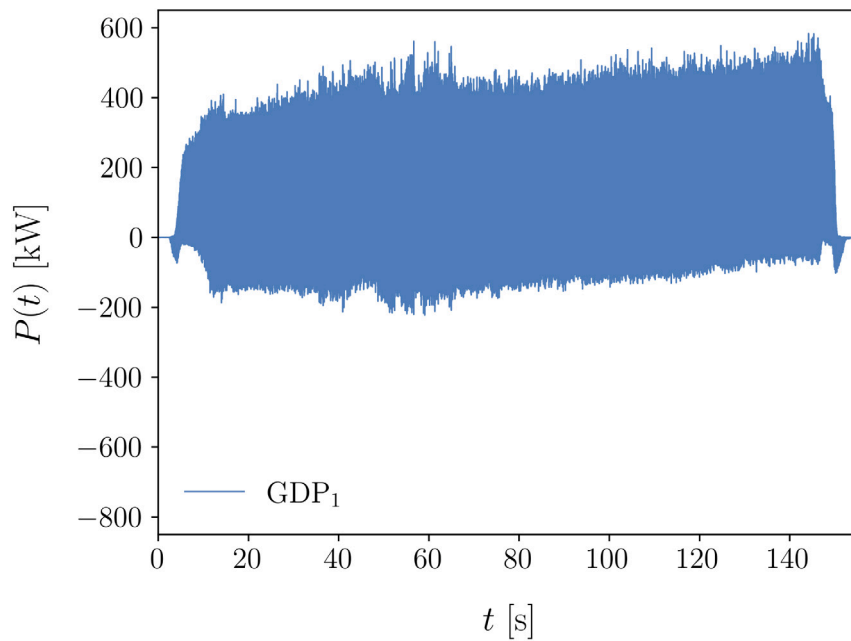


Fig. 18. Energy flux $P(t)$ at the top position for GDP₁.

us to claim that the cumulative energy flux can be used as an appropriate measure of efficiency in vibratory pile driving. Therefore, it is reasonable to quantify the penetration efficiency by the ratio of the cumulative energy flux and the energy input, as shown in Fig. 22.

6. Conclusions

In the area of offshore wind, alternatives techniques that reduce the environmental impact of monopile installation are essential for the further growth of the sector. To this end, a novel pile driving technique that aims at reducing the noise emissions and increasing the pile driving efficiency is developed. This method introduces a high-frequency torsional moment at the pile head, which in combination with the conventional low-frequency axial loading constitutes the Gentle Driving of Piles (GDP) method.

The objective of this paper is to characterize, based on the data collected during field tests, the driving efficiency of the vibratory installation methods. A new measure of this efficiency is proposed in this paper in terms of the cumulative energy flux normalized

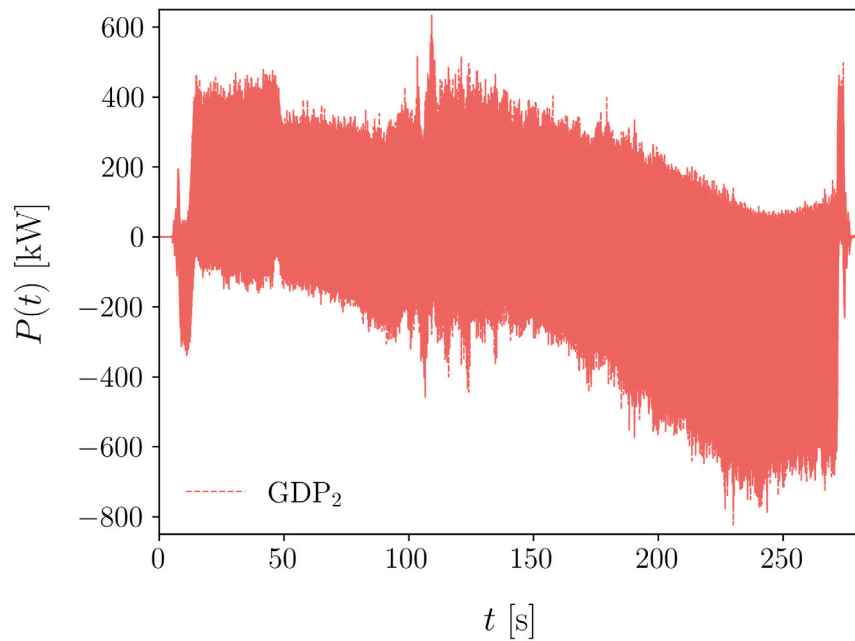


Fig. 19. Energy flux $P(t)$ at the top position for GDP₂.

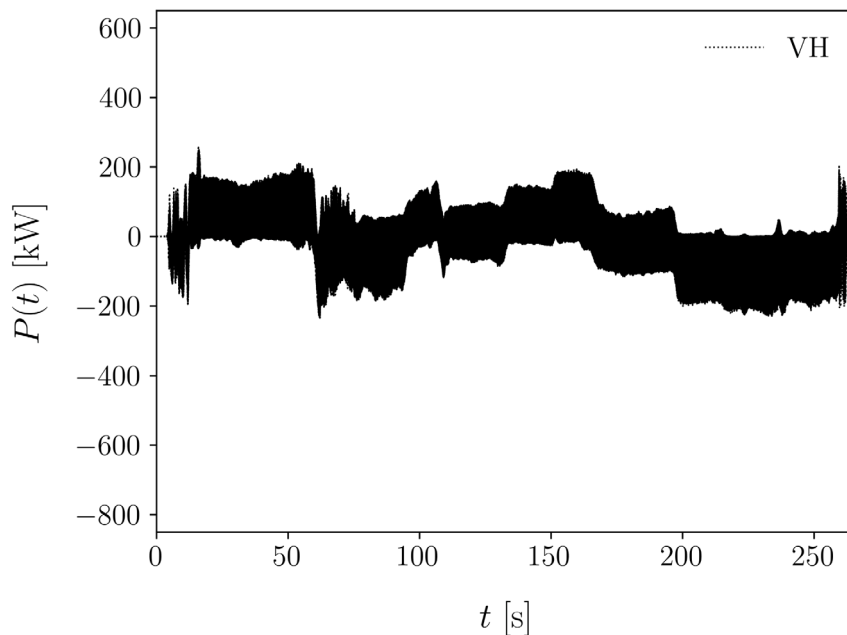


Fig. 20. Energy flux $P(t)$ at the top position for VH.

by the energy input. It has been found that this measure corresponds to a greater penetration rate and an energy-efficient pile installation.

The field campaign described in this paper provided a unique data set of three pile installation tests. During these tests, two piles were driven into the soil by means of the novel GDP method and one pile using axial vibro-driving. The data collected during the experimental campaign demonstrated, among other findings, the existence and effect of super-harmonics of the fundamental frequency of the shaker. Even though these super-harmonics were expected given the use of eccentric mass vibrators, it was not anticipated before that the pile vibrations at these super-harmonics will contain so high energy. The latter is of great importance

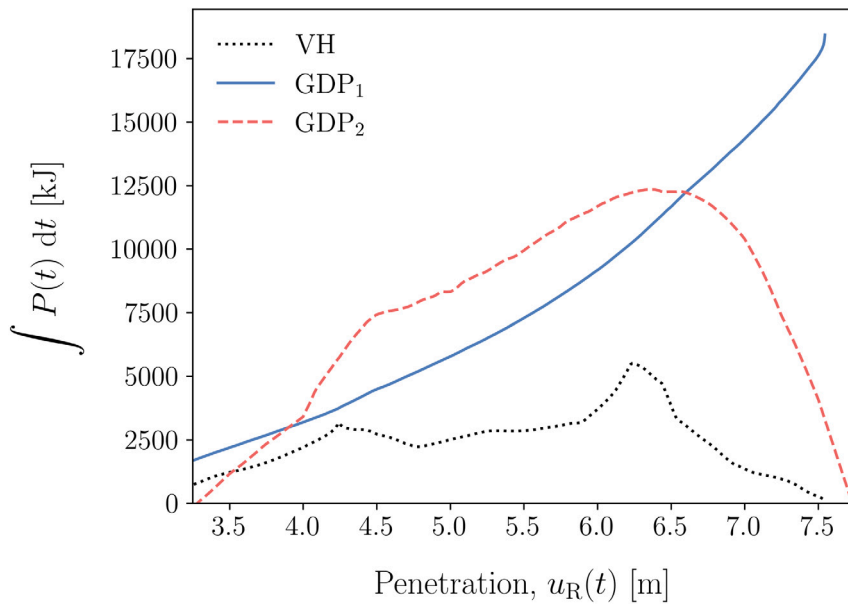


Fig. 21. Cumulative energy flux into VH and GDP piles, based on $\int P(t) dt$.

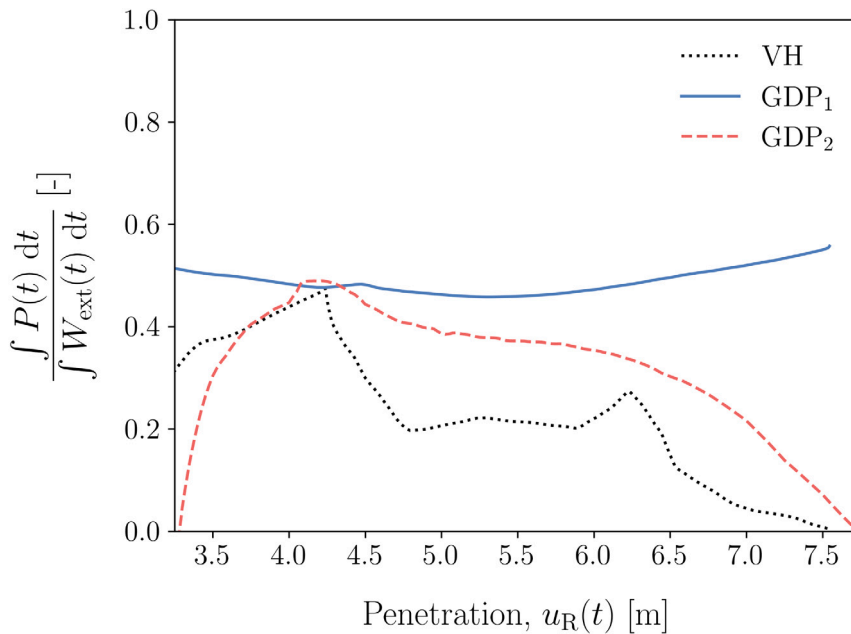


Fig. 22. Driving efficiency for the VH and GDP piles.

for the underwater noise generated during offshore pile driving and encourages further experimental and numerical investigations in the topic of vibratory pile driving.

CRedit authorship contribution statement

Sergio S. Gómez: Conceptualization, Methodology, Software, Validation, Investigation, Data curation, Writing – original draft. **Athanasios Tsetas:** Methodology, Validation, Investigation, Resources, Visualization, Writing – review & editing. **Andrei V. Metrikine:** Supervision, Writing – review & editing, Project administration, Funding acquisition.

Acknowledgments

This research is associated with the GDP project in the framework of the GROW joint research program. Funding from “Topsector Energiesubsidie van het Ministerie van Econsomische Zaken, The Netherlands” under grant number TE-HE117100 and financial/technical support from the following partners is gratefully acknowledged: Royal Boskalis Westminster N.V., The Netherlands, CAPE Holland B.V., Deltares, The Netherlands, Delft Offshore Turbine B.V., The Netherlands, Delft University of Technology, The Netherlands, ECN, The Netherlands, Eneco Wind B.V., The Netherlands, IHC IQIP B.V., The Netherlands, RWE Offshore Wind Netherlands B.V., The Netherlands, SHL Offshore Contractors B.V., The Netherlands, Shell Global Solutions International B.V., The Netherlands, Sif Netherlands B.V., The Netherlands, TNO, The Netherlands and Van Oord Offshore Wind Projects B.V, The Netherlands.

Appendix. Derivation of the energy flux based on the lagrangian formalism

In this section the Lagrangian form of equations of motion of a membrane shell, defined in the region $\Omega = \{a_i \leq x_i \leq b_i\}$ with the boundary Γ , are derived by means of the Hamilton–Ostrogradsky principle. The Lagrangian density function λ employing index notation is defined as:

$$\lambda = \lambda (t, x_i, u_i, \dot{u}_i, u_{i,j}) \tag{A.1}$$

where, u_i is the generalized coordinate, the $(,)$ denotes the spatial derivative, and the $(\dot{})$ denotes the time derivative. To obtain the Lagrangian form of the equation of motion and the boundary conditions, the variational principle is employed. To this end, let us first consider a perturbed displacement X_i of the real displacement u_i in the following form:

$$X_i(x_1, x_2, t) = u_i(x_1, x_2, t) + \varepsilon \xi_i(x_1, x_2, t) \tag{A.2}$$

where ε is the quantity of the perturbation and ξ_i is a normalized perturbation. Let us suppose that these two arbitrary displacements X_i and u_i describe the motions of the continuum during the time interval $\alpha < t < \beta$, and that the perturbations at the time extremes α and β are zero, such that:

$$\xi_i(x_1, x_2, \alpha) = \xi_i(x_1, x_2, \beta) = 0 \tag{A.3}$$

The Hamilton–Ostrogradsky principle states that:

$$\frac{d}{d\varepsilon} \left[\int_{\alpha}^{\beta} \int_{\Omega} \lambda \, d\Omega dt \right]_{\varepsilon=0} = 0 \tag{A.4}$$

and leads to:

$$\int_{\alpha}^{\beta} \left[\int_{\Omega} \left(\frac{\partial \lambda}{\partial u_i} \xi_i + \frac{\partial \lambda}{\partial \dot{u}_i} \dot{\xi}_i + \frac{\partial \lambda}{\partial u_{i,j}} \xi_{i,j} \right) d\Omega \right] dt = 0 \tag{A.5}$$

where the following relations that ensure uniqueness in Eq. (A.5) are used:

$$\begin{aligned} \frac{\partial \lambda}{\partial \dot{u}_i} \dot{\xi}_i &= \frac{\partial}{\partial t} \left(\xi_i \frac{\partial \lambda}{\partial \dot{u}_i} \right) - \xi_i \frac{\partial}{\partial t} \frac{\partial \lambda}{\partial \dot{u}_i} \\ \frac{\partial \lambda}{\partial u_{i,j}} \xi_{i,j} &= \frac{\partial}{\partial x_j} \left(\xi_i \frac{\partial \lambda}{\partial u_{i,j}} \right) - \xi_i \frac{\partial}{\partial x_j} \frac{\partial \lambda}{\partial u_{i,j}} \end{aligned} \tag{A.6}$$

Substituting the terms in Eq. (A.6) into Eq. (A.5), and applying the Gauss divergence theorem the following expression is obtained:

$$\int_{\alpha}^{\beta} \left\{ \int_{\Omega} \xi_i \left(\frac{\partial \lambda}{\partial u_i} + \frac{\partial}{\partial t} \frac{\partial \lambda}{\partial \dot{u}_i} + \frac{\partial}{\partial x_j} \frac{\partial \lambda}{\partial u_{i,j}} \right) d\Omega - \int_{\Gamma} \xi_i \left(\frac{\partial \lambda}{\partial u_{i,j}} \right) d\Gamma \right\} dt - \int_{\Omega} \xi_i \frac{\partial \lambda}{\partial u_i} \Big|_{\alpha}^{\beta} d\Omega = 0. \tag{A.7}$$

Setting to zero the integrand of the first integral in Eq. (A.7), we obtain the equation of motion in the Lagrangian form:

$$\frac{\partial \lambda}{\partial u_i} + \frac{\partial}{\partial t} \frac{\partial \lambda}{\partial \dot{u}_i} + \frac{\partial}{\partial x_j} \frac{\partial \lambda}{\partial u_{i,j}} = 0 \tag{A.8}$$

The integrand of the boundary integral corresponds to the stress σ_{ij} at the boundaries expressed in the Lagrangian form:

$$\sigma_{ij} = - \frac{\partial \lambda}{\partial u_{i,j}} \tag{A.9}$$

The last integral vanishes at the limiting time moments α and β as described in Eq. (A.3). The balance of mechanical energy density of a conservative system with no external energy reads:

$$\frac{de}{dt} + \nabla \cdot \mathbf{s} = 0 \tag{A.10}$$

where e is the mechanical energy density. The energy flux \mathbf{s} is expressed in the Lagrangian form of standard stress tensor σ_{ij} and the velocity field \dot{u}_i as:

$$s_j = -\sigma_{ij} \dot{u}_i = \frac{\partial \lambda}{\partial u_{i,j}} \dot{u}_i \tag{A.11}$$

References

- [1] M.D. Esteban, J.J. Diez, J.S. López, V. Negro, Why offshore wind energy? *Renew. Energy* 36 (2) (2011) 444–450.
- [2] S. Rodrigues, C. Restrepo, E. Kontos, R.T. Pinto, P. Bauer, Trends of offshore wind projects, *Renew. Sustain. Energy Rev.* 49 (2015) 1114–1135.
- [3] A. Cabboi, M. Seegeren, H. Hendrikse, A. Metrikine, Vibration-assisted installation and decommissioning of a slip-joint, *Eng. Struct.* 209 (2020) 109949.
- [4] Z. Zhang, B. Fitzgerald, Tuned mass-damper-inerter (TMDI) for suppressing edgewise vibrations of wind turbine blades, *Eng. Struct.* 221 (2020) 110928.
- [5] C. Sun, V. Jahangiri, Fatigue damage mitigation of offshore wind turbines under real wind and wave conditions, *Eng. Struct.* 178 (2019) 472–483.
- [6] M.D. Esteban, J.-S. López-Gutiérrez, V. Negro, Gravity-based foundations in the offshore wind sector, *J. Mar. Sci. Eng.* 7 (3) (2019) 64.
- [7] L. Ramírez, D. Fraile, G. Brindley, Offshore wind in Europe: Key trends and statistics 2019, Technical Report, WindEurope, Brussels, Belgium, 2020.
- [8] Z. Jiang, Installation of offshore wind turbines: A technical review, *Renew. Sustain. Energy Rev.* 139 (2021) 110576.
- [9] K. Thomsen, *Offshore Wind: A Comprehensive Guide To Successful Offshore Wind Farm Installation*, Academic Press, 2014.
- [10] A. Tsouvalas, Underwater noise emission due to offshore pile installation: A review, *Energies* 13 (12) (2020) 3037.
- [11] A.V. Metrikine, A. Tsouvalas, M.L.A. Seegeren, A.S.K. Elkadi, F.S. Tehrani, S.S. Gómez, R. Atkinson, F. Pisanò, E. Kementzetzidis, A. Tsetas, T. Molenkamp, K. van Beek, P. de Vries, GDP: A new technology for Gentle Driving of (mono)Piles, in: *Proceedings of the 4th International Symposium on Frontiers in Offshore Geotechnics*, Austin, TX, USA, 16–19 August 2020, 2020.
- [12] A. Tsetas, S.S. Gómez, A. Tsouvalas, K. van Beek, F.S. Tehrani, E. Kementzetzidis, F. Pisanò, A. Elkadi, M. Seegeren, T. Molenkamp, A.V. Metrikine, Experimental identification of the dynamic behaviour of pile-soil system installed by means of three different pile-driving techniques, in: *Proceedings of the XI International Conference on Structural Dynamics, EUROSDYN 2020, Vol. II, European Association for Structural Dynamics*, 2020, pp. 3005–3015.
- [13] J.-B. Han, S.-Y. Hong, J.-H. Song, Energy flow model for thin plate considering fluid loading with mean flow, *J. Sound Vib.* 331 (24) (2012) 5326–5346.
- [14] A. Alberdi-Muniain, N. Gil-Negrete, L. Kari, Direct energy flow measurement in magneto-sensitive vibration isolator systems, *J. Sound Vib.* 331 (9) (2012) 1994–2006.
- [15] W.O. Wong, X. Wang, L. Cheng, Modal power flow analysis of a damaged plate, *J. Sound Vib.* 320 (1–2) (2009) 84–100.
- [16] K. Graff, *Wave Motion in Elastic Solids*, Dover Publications, 1991.
- [17] A.W. Leissa, *Vibration of Shells*, Scientific and Technical Information Office, National Aeronautics and Space Administration, 1973.
- [18] P.M. Morse, H. Feshbach, *Methods of Theoretical Physics*, McGraw-Hill Book Company, Inc., New York, 1953.
- [19] M. Randolph, S. Gourvenec, *Offshore Geotechnical Engineering*, CRC Press, 2017.
- [20] S. Henke, J. Grabe, Field measurements regarding the influence of the installation method on soil plugging in tubular piles, *Acta Geotech.* 8 (3) (2013) 335–352.
- [21] A. Tsetas, A. Tsouvalas, A.V. Metrikine, Installation of large-diameter monopiles: introducing wave dispersion and non-local soil reaction, *J. Mar. Sci. Eng.* 9 (3) (2021) 313.
- [22] M. Jamiolkowski, D. Lo Presti, M. Manassero, Evaluation of relative density and shear strength of sands from CPT and DMT, in: *Soil Behavior and Soft Ground Construction*, 2003, pp. 201–238.
- [23] A.E. Holeyman, Soil behavior under vibratory driving, in: *Proceedings of the International Conference on Vibratory Pile Driving and Deep Soil Compaction, Transvib 2002*, 2002, pp. 3–19.
- [24] A. Holeyman, V. Whenham, Critical review of the Hypervib1 model to assess pile vibro-drivability, *Geotechn. Geol. Eng.* 35 (5) (2017) 1933–1951.